

TECHNICAL DESIGN OF THE ESS FACILITY

S. Peggs, ESS, Lund, Sweden,
for the ESS Technical Design Report contributors*

FACILITY OVERVIEW

ESS will deliver its first protons to a solid, rotating tungsten target in 2019, which will in turn generate slow neutrons for delivery to an initial suite of seven neutron scattering research instruments. Full design specifications will be reached in 2025, with a 5 MW beam and 22 research instruments, serving the European neutron research community (currently including about 6000 researchers) until 2065. The end of the three year-long pre-construction phase is marked by the April 2013 publication of the *Technical Design Report* [1], signalling the readiness of the project to move into construction, followed by the start of early operations in 2017. Table 1 records the high level ESS parameters., while Figure 1 provides a drawing of the layout of the main components of the facility.

Table 1: High level ESS parameters

Parameter	Unit	Value
Average beam power	MW	5
Number of target stations		1
Number of instruments		22
Number of beam ports		48
Number of moderators		2
Separation of ports	degrees	5
Proton kinetic energy	GeV	2.5
Average macro-pulse current	mA	50
Macro-pulse length	ms	2.86
Pulse repetition rate	Hz	14
Max. accel. cavity surface field	MV/m	40
Linac length (w/o 100 m upgrade)	m	482.5
Annual operating period	h	5000
Reliability	%	95

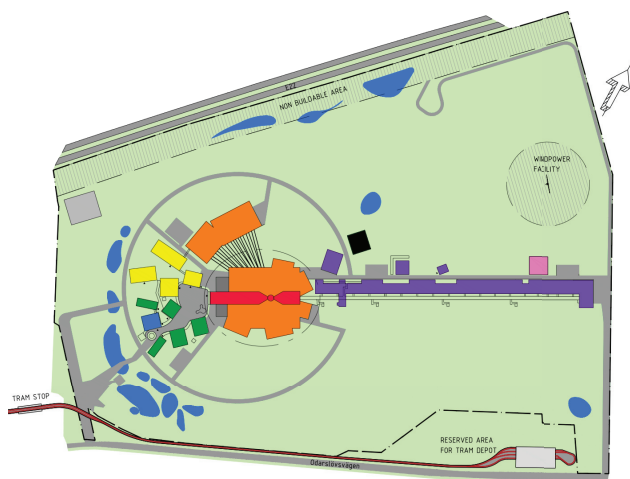


Figure 1: ESS facility components. Yellow: Labs. Orange: Instrument halls. Red: Target station. Purple: Accelerator. Blue: Reception. Green: Offices. Black: Utilities.

The specialised neutron beamlines and instruments will collectively generate vital information complementary to other methods, such as the X-rays provided by the MAX IV synchrotron that will be ESS’s immediate neighbour. Figure 2 shows the reference suite of 22 instruments, selected for illustrative purposes from the 40-odd instrument concepts presently under development. The instruments that actually will be built are likely to be quite different from those in the reference suite, since instrument selection will take place in a staged process, starting in 2013, that will permit ESS to choose state-of-the-art designs that are scientifically relevant when they enter user operation.

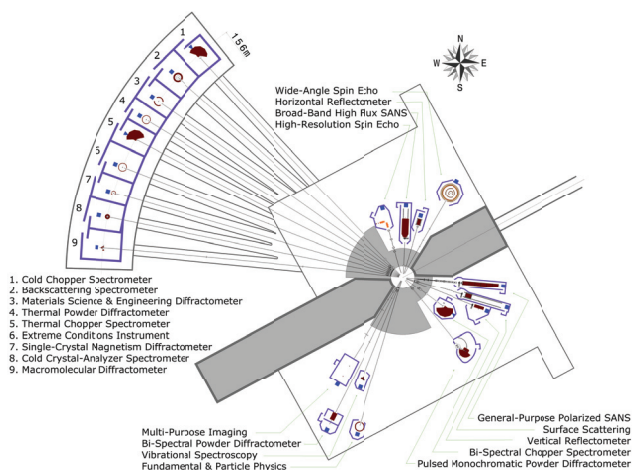


Figure 2: Neutron beamlines and instruments in the reference instrument suite that is used for illustrative purposes.

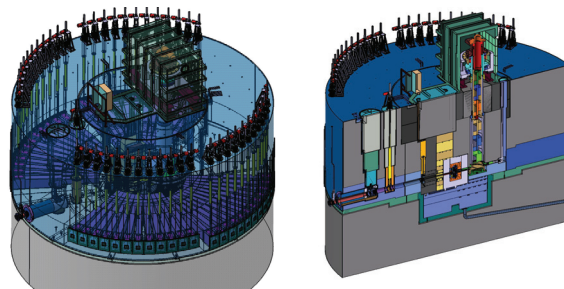


Figure 3: Monolith layout. Left: Perspective view. Right: Side view along the vertical plane of the proton beam.

* https://dl.dropboxusercontent.com/u/24187786/ess/TDR_Contributors.pdf

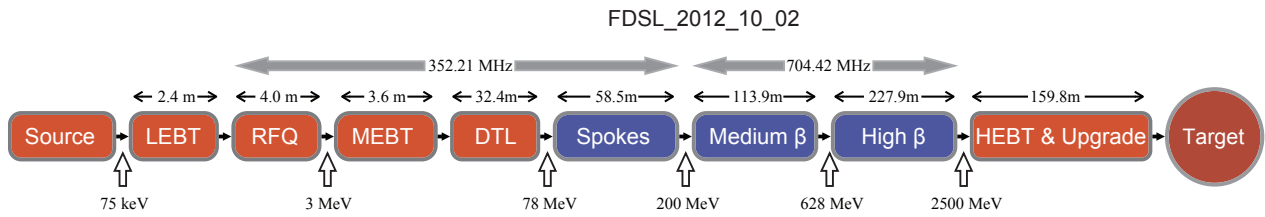


Figure 4: Block diagram of the FDSL_2012_10_02 accelerator lattice, showing section lengths, input and output energies, and frequencies. Orange items are normal conducting, while blue items are superconducting.

Figure 3 shows how the tungsten target is rotated by a vertical shaft that is offset from the monolith axis, connected to a drive unit on top of the monolith. Neutron moderators and reflectors are just above and below the target, on the monolith axis that is the centre of neutron production. A proton beam window (PBW) separates accelerator vacuum (on the left) from the atmospheric pressure helium inside the monolith. Several diagnostic devices monitor the proton beam footprints on the PBW and on the target.

Table 2: Tank, cavity, cell and cryomodule parameters

Section	Geom. β	Tanks or modules	Cells or cavities	Temp. [K]
RFQ		4		300
DTL		4	156	300
Spoke	0.50	14	28	≈ 2
Medium- β	0.67	15	60	≈ 2
High- β	0.92	30	120	≈ 2

ACCELERATOR

Figure 4 shows the linac layout. Proton beam from the electron cyclotron resonance ion source passes through a low energy beam transport (LEBT) section to the radio-frequency quadrupole (RFQ) for bunching and acceleration, as illustrated in Figure 5 (top). The beam from the RFQ is transported and matched through a medium energy beam transport (MEBT) section shown in Figure 5 (bottom) to the normal conducting drift tube linac (DTL). Then it enters the spoke resonator and elliptical cavity sections of the superconducting linac, before being transported via the high energy beam transport (HEBT) section to the target.

Table 2 counts the spoke, medium- β and high- β cryomodules in the FDSL_2012_10_02 lattice. Figure 6 (top) shows two double-spoke resonators in a single cryomodule, while Figure 6 (bottom) show how 4 medium- β cryomodules connect from the tunnel (4 m underground) to the RF or klystron gallery at surface level.

Copyright © 2013 by JACoW — cc Creative Commons Attribution 3.0 (CC-BY-3.0)

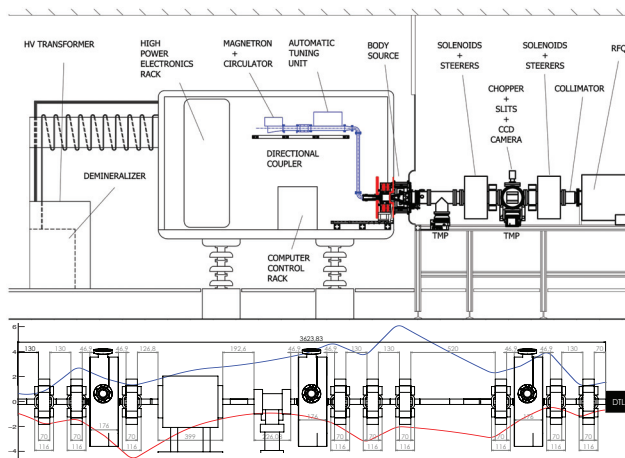


Figure 5: Top: Beam from the ion source passes through a chopper that incorporates beam emittance measurement slits, followed by a collimator just before entrance to the RFQ. Bottom: The MEBT contains 10 quadrupoles, 3 bunchers, and 3 collimators. RMS beam sizes are also plotted, in mm: horizontal in blue, vertical in red.

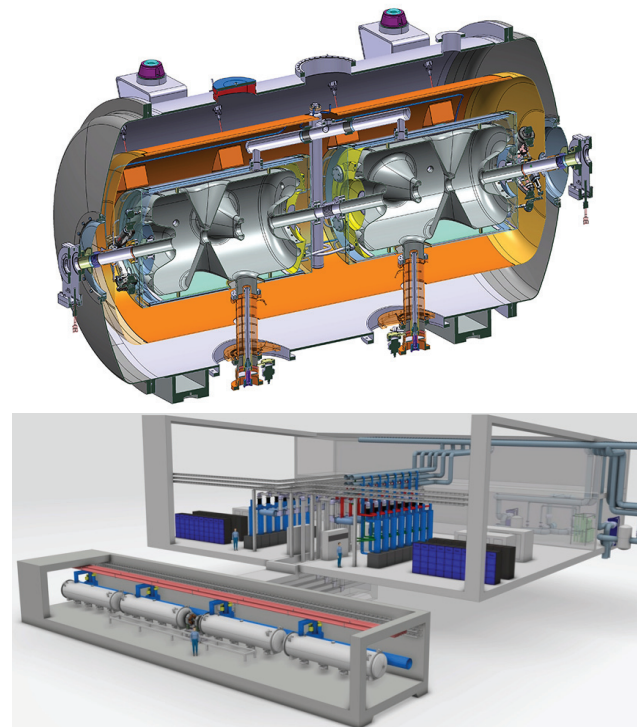


Figure 6: Top: A cryomodule with 2 double spoke cavities. Bottom: Medium- β cryomodules with 4 elliptical cavities connect through a waveguide stub to the RF gallery.

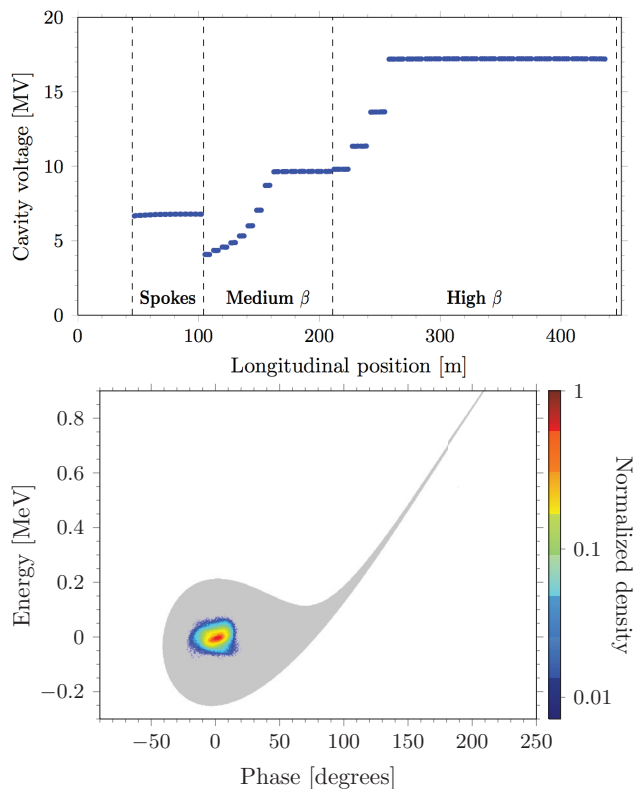


Figure 7: Top: Cavity voltage versus distance along the linac. Bottom: Longitudinal acceptance, referred to the entrance of the DTL. The actual beam out of the MEBT is represented by the coloured distribution at the centre.

BEAM OPTICS & DYNAMICS

The FDSL_2012_10.02 beam optics design is mature and robust, with very small emittance growth, and with margins and tolerances to faults and parameter variations that are balanced against cost and schedule issues. The beam has to pass smoothly between linac structures (RFQ, MEBT, DTL, superconducting linac and HEBT) that have been designed somewhat separately by different collaboration partners. Some interface adjustments have been made during the last year to achieve this. For instance, the focusing towards the end of the RFQ has been adjusted to better match the MEBT, and one tank has been added to the DTL.

Figure 7 (top) shows the cavity voltage, defined as

$$V = \int E(z) \cos\left(\frac{2\pi z}{\beta\lambda}\right) dz \quad (1)$$

versus distance at optimum β (i.e. at maximum transit-time factor). The gradual increase in voltage at the beginning of each section matches the longitudinal focusing and ensures a smooth evolution of the longitudinal phase advance per metre. End-to-end simulations generate the longitudinal acceptance shown in Figure 7 (bottom), at the entrance to the DTL. Only particles entering the DTL inside the grey area will reach the end of the linac. The actual beam – a 0.20π mm mrad Gaussian truncated at 4σ at the entrance

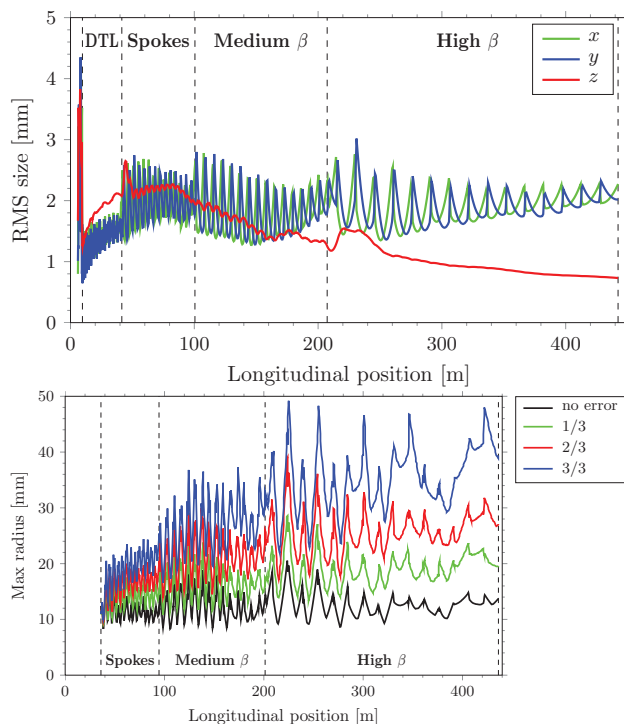


Figure 8: Top: RMS beam sizes from the MEBT to the end of the high- β section. Bottom: Maximum beam radius versus distance with increasing errors. Black, green, red and blue curves, respectively, represent error amplitudes at 0/3, 1/3, 2/3 and 3/3 of full strength.

of the RFQ – is represented by the coloured distribution at the centre. Beam sizes from end-to-end multi-particle simulations including space-charge are shown in Figure 8 (top). The emittance exchange and growth are less than 10% through the entire superconducting linac.

The linac configuration must be tolerant against static and dynamic variations in parameter values, and beam losses must remain (much) less than 1 W/m. The accelerator should be able to run even if some components fail. To address these issues, error studies and fault and failure analyses have been initiated. Figure 8 (bottom) shows simulations of the maximum radius of the proton along the linac for an ideal machine and for machines with various amplitudes of alignment and field errors.

ACKNOWLEDGEMENT

The TDR contributors and editors would like to acknowledge the sterling leadership and constant good humour of the outgoing ESS Director-General, Colin Carlile.

REFERENCES

- [1] S.Peggs (editor), “ESS Technical Design Report”, Lund, April 2013, ESS-doc-274, <http://europanspallationsource.se/documentation/tdr.pdf>